PLANETARY SCIENCE

A large meteoritic event over Antarctica ca. 430 ka ago inferred from chondritic spherules from the Sør Rondane Mountains

M. Van Ginneken[1,2,3]*[†‡], S. Goderis[2‡], N. Artemieva[4,5‡], V. Debaille[3], S. Decrée[1], R. P. Harvey[6], K. A. Huwig[6], L. Hecht[7,8], S. Yang[9], F. E. D. Kaufmann[7], B. Soens[2], M. Humayun[9], F. Van Maldeghem[2], M. J. Genge[10], P. Claeys[2]

Large airbursts, the most frequent hazardous impact events, are estimated to occur orders of magnitude more frequently than crater-forming impacts. However, finding traces of these events is impeded by the difficulty of identifying them in the recent geological record. Here, we describe condensation spherules found on top of Walnumfjellet in the Sør Rondane Mountains, Antarctica. Affinities with similar spherules found in EPICA Dome C and Dome Fuji ice cores suggest that these particles were produced during a single-asteroid impact ca. 430 thousand years (ka) ago. The lack of a confirmed crater on the Antarctic ice sheet and geochemical and ^{18}O-poor oxygen isotope signatures allow us to hypothesize that the impact particles result from a touchdown event, in which a projectile vapor jet interacts with the Antarctic ice sheet. Numerical models support a touchdown scenario. This study has implications for the identification and inventory of large cosmic events on Earth.

INTRODUCTION

Remnants of hypervelocity impact on Earth's surface are mainly preserved as impact craters, generally circular depressions resulting from asteroids large and/or dense enough to reach ground level without suffering substantial atmospheric disruption (1). Crater formation is accompanied by the production of a characteristic set of shock-metamorphic effects (e.g., shocked quartz or shatter cones) and formation of high-pressure mineral phases (e.g., coesite and stishovite) in target rocks, resolvable geochemical anomalies, and ejection of target/projectiles materials with high velocity (e.g., tektites and microtektites) (2). Identifying hypervelocity impacts in the geological record is relatively straightforward if one or several of these features are identified. However, impactors several tens up to 150 m in size are totally fragmented and vaporized during atmospheric entry, resulting in a low-altitude airburst, similarly to the Tunguska and Chelyabinsk events over Russia in 1908 and 2013, respectively (3–5). Observation by direct eye witness accounts and indirect infrasound, seismic, video cameras, and numerical modeling of medium-sized airbursts have shown that these impacts represent a notable fraction of the extraterrestrial material accreted to Earth, with Tunguska-like

events occurring once every 100 to 10,000 years, which is orders of magnitude more frequent than large crater-forming impacts (6). However, evidence of these events is scarce in the geological record, principally due to difficulty in identifying and characterizing potential residues (7). Finding evidence of these low-altitude meteoritic events thus remains critical to understanding the impact history of Earth and estimating hazardous effects of asteroid impacts. In recent years, meteoritic ablation debris resulting from airburst events have been found in three different locations of Antarctica. The material found at Miller Butte (Northern Victoria Land), Dome Concordia, and Dome Fuji all appears to have been produced during a Tunguska-like airburst event 480 thousand years (ka) ago (7–9). Here, we present the discovery of extraterrestrial particles formed during a significantly larger event recovered on the summit of Walnumfjellet (WN) within the Sør Rondane Mountains, Queen Maud Land, East Antarctica (Fig. 1). The characteristic features of the recovered particles attest to an unusual type of touchdown event, intermediate between an airburst and a crater-forming impact, during which the high-velocity vapor jet produced by the total disruption of an asteroid reached the Antarctic ice sheet.

RESULTS

The igneous particles studied in this work (N = 17) are dark black, subrounded to perfectly spherical. About half the particles are compound spherules consisting of two or more coalesced spherules (Fig. 2 and fig. S1). Scanning electron microscopy observations of polished sections of the particles indicate quench textures similar to S-type cosmic spherules (10). The mineralogy of the particles mainly consists of olivine and iron spinel, with minor interstitial glass. We subdivided the particles into four groups on the basis of their textures and spinel content: (i) spinel-rich (SR) particles (N = 9) characterized by abundant octahedral, cruciform and/or dendritic spinel (≥17% volume), and skeletal and/or euhedral olivine (Fig. 2, A and C, and fig. S1, A to F); (ii) spinel-poor (SP) particles (N = 5) characterized by large (>10 μm) skeletal or euhedral crystals of olivine with minor

[1]Belgian Geological Survey, Royal Belgian Institute of Natural Sciences, 1000 Brussels, Belgium. [2]Analytical, Environmental and Geo-Chemistry, Vrije Universiteit Brussel, 1050 Brussels, Belgium. [3]Laboratoire G-Time, Université Libre de Bruxelles, 1050 Brussels, Belgium. [4]Planetary Science Institute, 1700 East Fort Lowell, Suite 106, Tucson, AZ 85719, USA. [5]Institute of Geosphere Dynamics, Russian Academy of Sciences, Moscow 119334, Russian Federation. [6]Department of Geological Sciences, 112 A. W. Smith Building, Case Western Reserve University, Cleveland, OH 44106-7216, USA. [7]Museum für Naturkunde Berlin, Leibniz Institut für Evolutions und Biodiversitätsfoschung, Invalidenstraße 43, 10115 Berlin, Germany. [8]Institut für Geologische Wissenschaften, Freie Universität Berlin, Malteserstr. 74-100, D-12449 Berlin, Germany. [9]National High Magnetic Field Laboratory and Department of Earth, Ocean & Atmospheric Science, 1800 E Paul Dirac Dr., Tallahassee, FL 32310, USA. [10]Department of Earth Science and Engineering, Imperial College London, London SW7 2AZ, UK.

*Corresponding author. Email: m.van-ginneken@kent.ac.uk
†Present address: Center for Astrophysics and Planetary Science, School of Physical Sciences, Ingram Building, University of Kent, Canterbury CT2 7NH, UK.
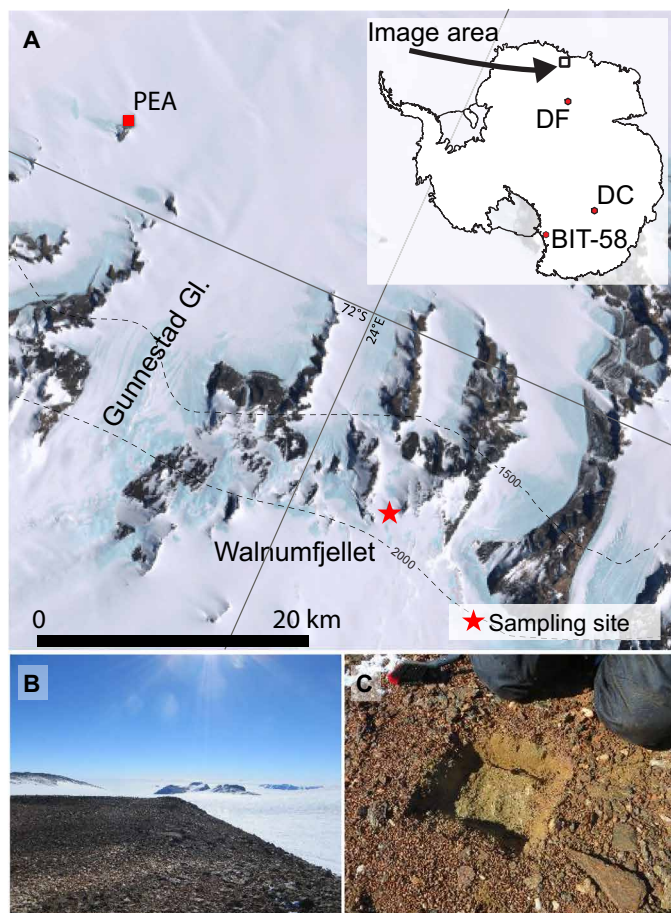‡These authors contributed equally to this work.

Fig. 1. Location of the sampling site in WN, Sør Rondane Mountains, Queen Maud Land, Antarctica. (**A**) Landsat image of the sampling site on the summit of WN, where the particles studied here were recovered, along with the Princess Elisabeth Antarctica (PEA). Inset shows the locations of Dome Fuji (DF), Dome Concordia (DC), and BIT-58 for comparison (8, 9, 24). The ages of the various horizons can be found in Table 1. (**B**) The flat glacially eroded summit of WN on the border of the Antarctic plateau. [10]Be exposure age of glacially eroded surfaces of WN range from 870 to 1740 ka (25). (**C**) The $30 \times 30 \times 10$ cm sampling site on top of WN. Landsat 7 image courtesy of the Landsat Image Mosaic of Antarctica (LIMA) project. Photo credit: Matthias van Ginneken, University of Kent.

cubic spinel content (<10% volume) (Fig. 2, B and D, and fig. S1, G and J); (iii) barred olivine (BO) particles ($N = 3$) that contain minor spinel content (<10% volume; fig. S1, H and K); and (iv) one cryptocrystalline (CC) compound particle consisting of two fused spherules exhibiting identical CC textures and moderate spinel content (~15% volume; fig. S1, I and L). The size of the particles does not vary significantly from one group to the other: 131 µm for the CC particle, 203 ± 115 µm for SR particles, 289 ± 93 µm for SP particles, and 308 ± 117 µm for BO particles.

The major element bulk composition of the individual particles obtained by electron probe microanalysis are reported in table S1 and plotted in Fig. 3. Elemental patterns show consistent and broadly chondritic compositions, albeit with variable depletions in alkali and in Cr, and severe depletion in S in all particles. Refractory elements Al, Ti, and Ca are depleted in SP particles WN-IP#8 (Walnumfjellet impact particle #8) and WN-IP#9 (WN-IP, Walnumfjellet Impact Particle; Fig. 3 and table S1). Focused beam electron microprobe

analyses show that olivine in SR particles is mostly iron poor (i.e., $Fa_{10\pm3}$), whereas it is iron rich in SP and BO particles (i.e., $Fa_{22\pm4}$ and $Fa_{21\pm5}$, respectively; table S2). The nickel content in olivine is always high and consistent throughout all particle types, with NiO = 2.78 $\pm$ 0.46 weight % (wt %) (table S2). In SR particles, spinel exhibits high-Mg and high-Ni concentrations (MgO = 8.12 to 12.26 wt %, NiO = 3.28 to 4.84 wt %; table S3), indicating important magnesioferrite and trevorite components, and minor magnetite. Conversely, spinel crystals exhibit lower Mg and Ni concentrations in SP particles (MgO = 1.77 to 1.99 wt %, NiO = 0.73 to 1.16 wt %). The bulk trace element composition of the particles, determined using laser ablation–inductively coupled plasma-mass spectrometry (LA-ICP-MS), is reported in table S4 and fig. S2, along with the bulk compositions of sediments from which they were extracted. Similarly to the major element chemistry, the CI-normalized flat pattern exhibited by most particles is suggestive of chondritic material. Enrichments up to ca. an order of magnitude of U, Th, and La (gray dashed lines in fig. S2) are observed and likely due to contamination by the local sediment. Conversely, we observe depletions in Zn and Pb to various extents, suggesting evaporative loss at high temperature. The oxygen isotopic compositions of the particles are characterized by highly negative $\delta^{18}O$, ranging from −35 to −52‰ (Fig. 4 and table S5). Similarly to the textural and chemical properties, the SR and SP particles display distinct $\delta^{18}O$ values, ranging from −44 to −28‰ and −52 to −45‰, respectively. The BO particles show a narrower range in $\delta^{18}O$ values, from −51 to −50‰. The CC particle displays the highest $\delta^{18}O$ value at −40‰. The $\Delta^{17}O$ is constant throughout all groups and ranges from −0.3 to −1.2‰.

DISCUSSION
Spherules resulting from a major meteoritic event on the East-Antarctic ice sheet
The chondritic bulk major and trace element chemistry and high Ni content demonstrate the extraterrestrial nature of the recovered particles (Fig. 3, fig. S2, and tables S1 and S4). The particles resemble S-type cosmic spherules, which are essentially composed of olivine, minor iron spinel, and interstitial glass (10). However, WN particles differ from cosmic spherules on several crucial properties. The high Ni concentrations of olivine (NiO = 2.00 to 3.31 wt %) record high oxidizing conditions relative to those determined for cosmic spherules (11). Compound spherules are not observed among cosmic spherules, as the probability for these spherules to coalesce during flight while still molten is negligible. Iron spinel in S-types cosmic spherules is mainly composed of magnetite ($Fe^{2+}Fe^{3+}_2O_4$), due to the relatively limited oxidizing conditions in the upper atmosphere (10, 12, 13). Increasing oxidizing conditions result in a higher Fe^{3+}/Fe_{tot} ratio (77 to 89) and, thus, a major magnesioferrite component, as observed in SR spherules [>80 wt %; $Mg(Fe^{3+})_2O_4$], whereas magnetite is a minor component (<10 wt %). Present spinel compositions are consistent with impact or meteoritic ablation spherules (2, 14–20). The spinel composition of SR spherules is also consistent with that of impact debris formed during an airburst event in the lower layers of the atmosphere (7). Sodium content is also higher than that observed in S-type spherules [$Na_2O < 1$ wt %; (11)] and consistent with impact spherules forming in a dense chondritic gas and/or in the pressured gas due to the presence of a bow shock during atmospheric entry (7). The SR spherules must have resulted from the atmospheric entry of a chondritic body large enough to reach the lower atmosphere. SP spherules exhibit low Fe^{3+}/Fe_{tot} values with
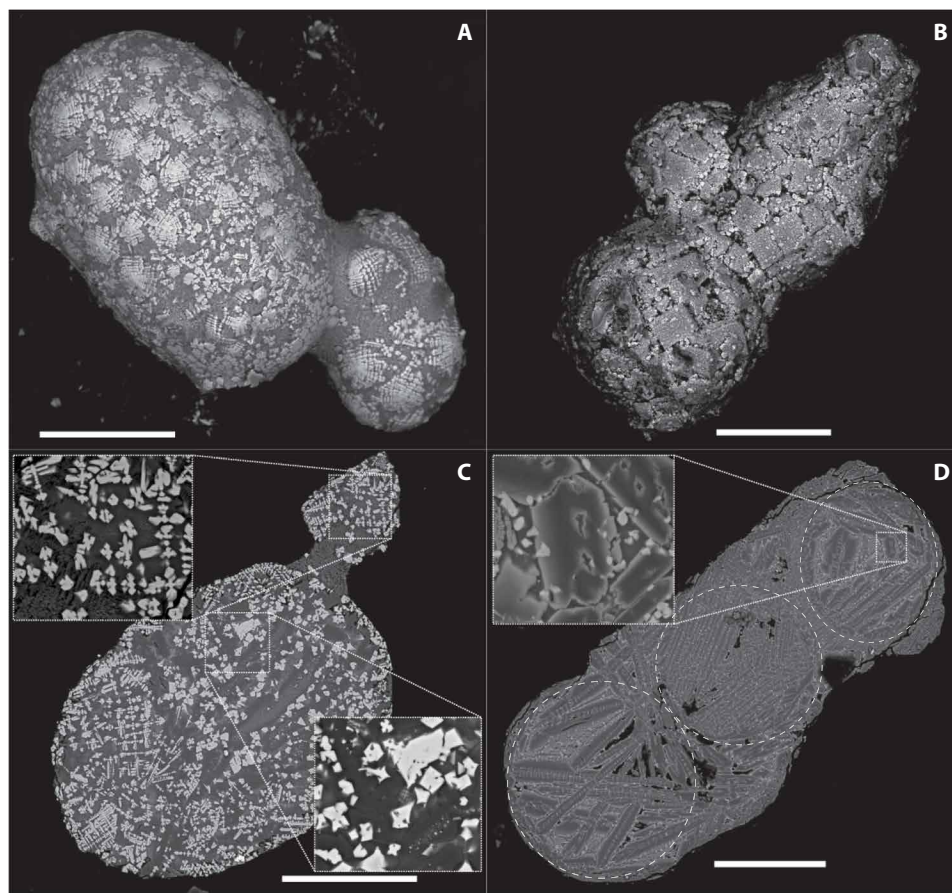
Fig. 2. Scanning electron backscattered images of WN particles. (**A**) WN-IP#12 (SR), which consists in skeletal Fe-poor olivine (Fa < 10), Fe spinel, and minor interstitial glass. (**B**) WN-IP#6 (SP), which consists of large skeletal Fe-rich olivine (Fa > 10), and minor Fe spinel and interstitial glass. (**C**) and (**D**) represent polished section of WN-IP#12 and WN-IP#6, respectively. Insets in (C) and (D) are close-ups showing the morphology of olivine and Fe spinel crystals. Scale bars, 100 μm.
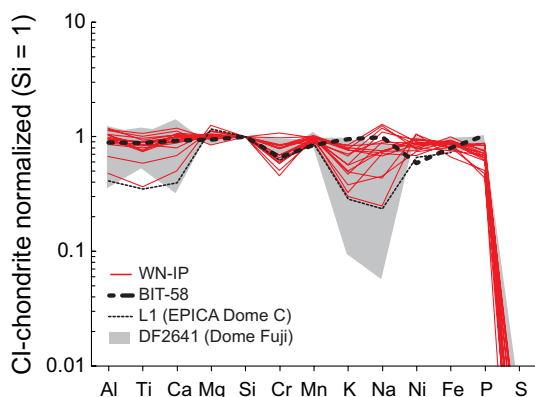

Fig. 3. Major element bulk compositions of the impact WN particles (WN-IP), normalized to CI-chondrite bulk composition (46). Bulk compositions of impact particles from BIT-58 (average), L1 from EPICA Dome C ice core (average), and DF2641 from Dome Fuji ice core (range for individual analyses) are shown for comparison. Elements are arranged in order of increasing volatility from left to right (47).

respect to cosmic spherules (i.e., $Fe^{3+}/Fe_{tot} = 60$ to 62 and 66 to 72, respectively). The bulk chemistry and unique petrologic properties of SR and SP particles suggest a paired origin. We will show below how SR and SP spherules can form simultaneously.

The WN particles share structural, textural, and chemical properties with microkrystites, which are spherules that condense from large impact plumes (2, 19). Their mafic chemistry suggests high contributions from the impactor, while the spherical and/or subspherical shapes and lack of vesicles suggest that they condensed within a vapor saturated impact plume. These characteristics contrast those of the more common microtektites, which are melt products mainly composed of target material that display aerodynamic shapes (e.g. teardrops, dumbbells) typical of ballistic flight (2, 21–23). Formation through condensation in a dense plume is thus favored for the WN particles, as opposed to formation as melt products rapidly ejected along ballistic trajectories from the impact area.

In the Antarctic ice record, several occurrences of microkrystite-like dust layers have been recognized: the ~2.8-Ma-old BIT-58 dust horizon close to Allan Hills [76°43′0″S, 159°40′0″E; (24)] and two extraterrestrial dust horizons in the EPICA (European Project for Ice Coring in Antarctica) Dome C [i.e., L1 and L2; 75°06′S to 123°21′E; (8)] and Dome Fuji ice cores [i.e., DF2641 and DF2691;
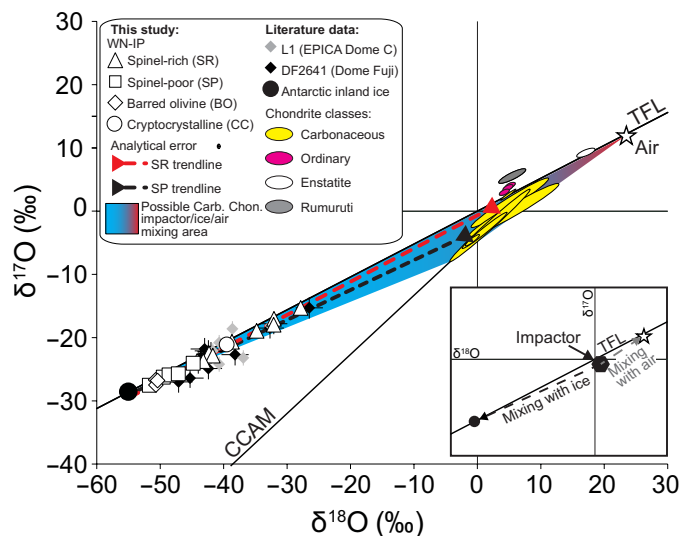
Fig. 4. δ^{17}O versus δ^{18}O diagram (values in ‰ versus V-SMOW) for WN particles, DF2641 particles from the Dome Fuji ice core (9), and L1 particles from the EPICA Dome C ice core (48). Antarctic inland ice values from (26) and tropospheric oxygen values from (32). Bulk isotopic compositions of chondritic meteorites are represented in rounded colored shaded areas, including carbonaceous chondrites [i.e., below the terrestrial fractionation line (TFL)], ordinary and Rumuruti chondrites (i.e., above the TFL), and enstatite chondrites (i.e., on the TFL) (27–29). The blue/red shaded areas represent hypothetical mixing area between a carbonaceous chondritic impactor, Antarctic inland ice (blue), and atmospheric oxygen (red). Trend lines for SR and SP WN particles are in red and black, respectively, and broadly represent mixing lines pointing to increasing mixing with ice. A larger deviation from the TFL means less interaction with atmospheric oxygen. Inset: The effects of oxygen isotopic exchange of a chondritic impactor with Antarctic ice and atmospheric air.

77°19′S to 39°42′E; (9)]. The dust horizons in the EPICA Dome C and Dome Fuji ice cores form the two pairs L1/DF2641 and L2/DF2691, which record two distinct cosmic events that occurred ca. 430 and 480 ka ago, respectively (8, 9). The BIT-58 particles formed during a single meteoritic event and exhibit a range in mineralogy and textures similar to those of our particles, albeit with some metals and sulfides in the glassy mesostasis (Table 1 and fig. S3) (24). These observations strongly support formation of WN particles during a single event. An absolute age for WN particles could not be determined. However, the ^{10}Be exposure ages of glacially eroded surfaces of the WN mountains range from 870 to 1740 ka old (25). The altitude of the WN particle collection surface suggests an exposure age of at least 870 ka and likely closer to 1740 ka. Therefore, the age and slight mineralogical incompatibilities prevent pairing with BIT-58, suggesting that both events are distinct.

The WN particles also bear remarkable resemblance to L1/DF2641 particles, whereas they are clearly distinct from L2/DF2691 particles (Table 1) (8, 9). Figure 3 and fig. S4 show that the observed chemical patterns of WN particles match well with the patterns exhibited by the L1/DF2641 particles. The bulk major compositions of WN particles do not appear to be controlled by the modal mineralogy of the particles, except for marked depletions in Na, K, Al, Ti, and Ca in two SP particles. These two particles are characterized by the largest olivine grains (up to 100 μm) and olivine modal abundance (~75% volume). Similar elemental depletions are observed in L1 particles and in some DF2641 particles (8, 9). Particles from the EPICA ice core show a relatively high modal abundance of olivine,

similar to SP particles. The observed depletions in these particles are likely due to the overabundance of olivine, which is not a carrier for these elements, thus favoring Mg, Fe, and Si. The high Si content in iron spinel in DF2641 particles suggests an overlap with surrounding silicate phases, preventing a precise calculation of Fe^{3+}/Fe_{tot} values and, thus, comparison with spinels in WN particles.

DF2641 particles exhibit negative δ^{18}O ranging from −27 to −47‰, similar to WN particles. The concentrations of grains, several orders of magnitude higher than the normal flux of cosmic spherules, coupled with their coeval age and chemistry indicate that L1 and DF2641 formed during a single large impact over the East Antarctic ice sheet (7–9). Negative δ^{18}O values in DF2641 particles are thought to result from the interaction of the particles with vapor characterized by Antarctic ice values at high temperature (9). As mentioned above, WN particles were deposited over the last 870 ka ago, which is compatible with the deposition time of L1 and DF2641 particles. The common petrological, chemical, and isotopic characteristics of the WN particles and L1/DF2641 particles, coupled with their age compatibility, suggest that they formed during the same event, thereby documenting a major meteoritic event over most of the Antarctic continent that occurred ca. 430 ka ago.

Nature of the impactor

Figure 4 shows that the oxygen isotopic signatures of WN particles plot between chondritic and inland Antarctic ice values along the terrestrial fractionation line (TFL) (26). This negative δ^{18}O is outside the range of chondritic materials and suggests that they have exchanged oxygen with ice during either formation or subsequent weathering (27–29). The silicate fraction of the particles does not show evidence of leaching and/or topotactic mineral replacement typical of terrestrial alteration, indicating no notable interaction with liquid water during weathering (30). In addition, oxygen isotopic compositions of cosmic spherules recovered from the summits of nunataks exposed for ca. 3 to 4 Ma ago show no evidence of isotopic exchange with seasonal snow (23, 31). This indicates that WN particles cannot have inherited their unique oxygen isotopic signatures during their storage in the Antarctic environment but rather during the impact event responsible for their formation.

The oxygen isotope compositions of WN particles exhibit several important characteristics (Fig. 4): (i) All values are close to the TFL, (ii) all values are below TFL (negative Δ^{17}O, which represents the deviation from the TFL), and (iii) all values are within δ^{18}O values of Antarctic inland ice (26). These characteristics allow several interpretations on the original composition of the precursor extraterrestrial material and the degree of mixing involved. We assume three discrete sources of oxygen as end members in the mixing occurring during the impact: (i) the chondritic impactor, (ii) Antarctic ice, and (iii) atmospheric air. Since Antarctic ice and atmospheric oxygen both have values very close to TFL (26, 32), the negative Δ^{17}O of the WN particles can only be produced by mixing between ice and/or air with a starting chondritic material having even lower Δ^{17}O. Consequently, a carbonaceous chondrite impactor rather than an ordinary chondrite body can be preferred as shown by the blue shaded area in Fig. 4. It is also possible to discount a CI chondrite precursor.

The oxygen isotope compositions also allow the degree of mixing between ice, air, and the impactor to be constrained. The low δ^{18}O values of the WN particles are close to Antarctic inland ice and demonstrate that ice-derived oxygen predominates over impactor or air-derived oxygen. We infer the degree of mixing from their

Table 1. Main properties of impact spherules from Antarctica. SR, spinel-rich; SP, spinel-poor; BO, barred olivine; CC, cryptocrystalline; DM, glassy dominated by dendritic magnesioferrite.

Sample	Locality	Coordinates	Age (ka ago)	Types	Size (μm)	Shape
WN	Walnumfjellet	72°07′S, 24°12′E	<870	SR, SP, BO, and CC	93 to 473	Spherical + subspherical
L1*	Dome Concordia	75°06′S, 123°21′E	434	SR and SP	Up to 100 μm	Angular (SP) + spherical (SR)
DF2641[†]	Dome Fuji	77°19′S, 39°42′E	434 ± 6	SR and SP	Up to 100 s μm	Subspherical
L2*	Dome Concordia	75°06′S, 123°21′E	481	DM	Submicrometer: 25 μm	Spherical
DF2691[†]	Dome Fuji	77°19′S, 39°42′E	481 ± 6	DM	Submicrometer: 15 μm	Spherical
MB[‡]	Miller Butte	72°42′S, 160°14′E	481	Mainly DM	Submicrometer: 65 μm	Spherical
BIT-58[§]	Allan Hills	76°43′S, 159°40′E	2.8×10^3	SR, SP, BO, and DM	Up to 100 μm	Angular (SP) + spherical (SR)

Sample	Mineralogy	Spinel morphology	Olivine morphology	Fa (olivine)	δ^{18}O (‰)
WN	Olivine + glass + Fe spinel	Cruciform + dendritic + cubic	Porphyritic + skeletal + barred	7 to 69	−51 to −32
L1*	Olivine + glass + Fe spinel	Cruciform + dendritic	Porphyritic + skeletal	~10 to 50	−38 to −21[∥]
DF2641[†]	Olivine + glass + Fe spinel	Cruciform + dendritic	Porphyritic + skeletal + barred	26 to 85	−47 to −27
L2*	Glass + Fe spinel	Dendritic	–	–	−17 to −10[∥]
DF2691[†]	Olivine + glass + Fe spinel	Dendritic	Dendritic	~10 to 50	–
MB[‡]	Olivine + glass + Fe spinel	Cruciform + dendritic + cubic	Skeletal + barred	14 to 21	3 to 6
BIT-58[§]	Olivine + glass + Fe spinel + Fe metal	Cruciform + dendritic + cubic	Porphyritic + skeletal + barred	17 to 24	–

References: *(8),   †(9),   ‡(7),   §(24),   ∥(48).

range at ~95 to ~50% by mass ice-derived oxygen. SR spherules have the highest δ^{18}O and thus have experienced less exchange with Antarctic ice. The more negative Δ^{17}O of WN particles than air and ice testifies to the impactor-derived fraction of oxygen in the particles. The relative fraction of air/impactor oxygen is difficult to conclusively specify since it depends on the initial impactor composition. If we assume an impactor having carbonaceous chondrite isotopic compositions (i.e., Δ^{17}O < 0‰), then a mixture of ice and impactor-derived oxygen will result in WN particles plotting in the blue shaded area in Fig. 4. The mixing line for SR spherules (i.e., red dashed trendline) falls above the mixing line formed by SP spherules (i.e., black dashed trendline), suggesting a lower Δ^{17}O impactor contribution in the former with respect to the latter and, thus, more mixing with air. Conversely, the lowest δ^{18}O WN particles (i.e., SP) exhibit larger Δ^{17}O deflections from TFL, providing some evidence, albeit at the limits of analytical certainty, that mixing with air decreases as mixing with ice increases. We discuss the large degree of ice-derived oxygen compared with impactor or air below in terms of the physical conditions of the impact scenario.

A touchdown event leading to the formation of the WN impact spherules

The discovery of unusual impact particles covering such a large area in Antarctica is anomalous. Known impact spherule layers in the geological record are usually associated with impact-cratering events (2). Examples of particles produced during airbursts events are rare, with the notable exceptions being the 480-ka-old event over Antarctica mentioned earlier (7, 9). DF2641 impact spherules recovered in the Dome Fuji ice core were also supposedly produced during a large airburst event over Antarctica ca. 430 ka ago (9). However, none of the proposed scenarios can account for the anomalous oxygen isotopic signature. The purely chondritic composition of WN particles precludes mixing with target rocks and thus implies the impact was not associated with a crater penetrating into crustal rocks (fig. S5). An event that generated a crater on the ice sheet may also be excluded, since no structure several hundreds of meters in diameter has yet been identified. Conversely, an airburst scenario implies no interaction with Earth's surface, and thus only mixing with atmospheric oxygen (33). An alternative to these two scenarios is an

intermediate "touchdown event," in which a jet of melted and vaporized meteoritic material reaches the surface at high velocity, whereas its density is too low to form an impact crater.

The petrological and geochemical properties of WN particles provide important clues about their mode of formation. Particularly, cosmic spinel is a good recorder of the ambient oxygen fugacity at the time of its crystallization as characterized by the ratio Fe^{3+}/Fe_{tot} (15). SR spherules have a Fe^{3+}/Fe_{tot} [76 to 88 atomic percent (at %)] similar to fusion crusts of meteorites (75 to 90 at %) and higher than micrometeorites (<75 at %). This is consistent with their formation in the lower atmosphere at high oxygen fugacity [<40 km; $fO_2 >> 10^{-6}$ atmosphere (atm)] rather than the high atmosphere (i.e., >80 km; $fO_2 < 10^{-6}$ atm). In contrast, SP spherules exhibit Fe^{3+}/Fe_{tot} (60 to 62 at %) that imply formation under more reducing conditions.

The quenched textures of SR and SP spherules indicate cooling in a matter of seconds, similar to both cosmic spherules and meteorite ablation spheres. These particles could not, therefore, have formed as cosmic spherules in the upper atmosphere since they would have cooled long before reaching Antarctic ice and would not have experienced isotopic exchange of oxygen with ice.

Formation in an impact plume could explain the occurrence of both SR and SP spherules at the same locality and is the simplest explanation for their morphological, mineralogical, and isotopic properties. Approximately half the particles are compound spherules, which necessitates formation in a dense and turbulent plume in which interparticle collisions are common, and precludes formation as cosmic spherules. Although we might expect some composite particles among meteorite ablation debris, lower abundances would be expected owing to their rapid liberation and distribution over the meteoroid trail.

Experimental synthesis of cosmic spinel by melting chondritic material shows that changing fO_2 during spinel formation essentially results in Mg^{2+} and Ni^{2+} replacing Fe^{2+}, and Fe^{3+} replacing Al^{3+} and Cr^{3+}. Figure S6 shows that the compositional trend observed for spinels in SR and SP spherules fits a scenario involving the condensation of pure chondritic material within a plume having extremely heterogeneous oxidizing conditions. The higher abundance of spinel in SR spherules compared with SP spherules is consistent with higher oxidizing conditions in the former, as spinel abundance is mainly controlled by oxygen fugacity (14). Spinel in SR spherules implies interaction at high oxygen fugacity ($>10^{-2}$ atm) similar to meteorite fusion crusts and thus infer oxidation by air. Certainly, the intrinsic oxygen fugacity of carbonaceous chondrite gas is too low to account for such a degree of oxidation in spinel (i.e., $\log fO_2 \approx -9$ at 1200°C) (34). Conversely, the lower oxidizing conditions (i.e. $fO_2 < 10^{-6}$ atm) responsible for the formation of spinel in SP spherules implies a more limited interaction with atmospheric oxygen. In case of a touchdown event on ice, however, vaporization will inject pure H_2O vapor into the impact plume. At low temperatures, the abundance of free oxygen in H_2O vapor is small [0.16% dissociation at 1600 K and 0.1 MPa; (35)]. However, this abundance increases with temperature owing to thermal dissociation (6.1% dissociation of H_2O at 2200 K). The oxidizing potential of high-temperature water vapor is moderated by the production of H_2 and, at the highest temperatures, 2H. Given a sequestration of large amounts of free oxygen from high-temperature gas, for example, by condensation of silicate droplets, the remaining hydrogen is likely to cause reduction.

An increased interaction with atmospheric O_2 during the formation of SR spherules can explain their oxygen isotopic compositions

with respect to SP spherules. The $\delta^{18}O$ of SP spherules suggest almost complete (~80 to 95%) exchange with ice vapor, while exchange is lower (~50 to 80%) in SR spherules. The consistent Na_2O content in SR and SP spherules (table S1) implies that both spherule types experienced a similar degree of evaporation. Thus, their differences in $\delta^{18}O$ are unlikely to result strongly from mass-dependent fractionation [i.e., that shifts toward higher $\delta^{18}O$, as observed in cosmic spherules; (31)]. A more likely scenario is a dominant isotopic exchange between SR spherules and atmospheric oxygen, similarly to meteorite ablation spheres resulting from an airburst (33). Such an exchange accounts for an approximately 8‰ increase in $\delta^{18}O$ in meteorite fusion crusts (13). The relatively large available surface area available for isotopic exchange in impact spherules compared to fusion crusts may partly explain the large degree of isotopic exchange and account for the $\delta^{18}O$ difference observed between SR and SP spherules (~20‰). More significantly, silicates vaporize as SiO and O_2 molecules in the vapor phase (36); thus, large-scale exchange of oxygen is possible as vapor cools and condenses to form silicate melt spherules.

A touchdown event may reconcile both the spinel compositions and oxygen isotopes in SR and SP spherules. Assuming that SR spherules interacted early during their formation with atmospheric oxygen, as suggested by their spinel composition and oxygen isotopic signatures, a formation in the periphery of an impact plume seems likely. Conversely, the relatively low degrees of oxidation of spinel in SP spherules, coupled with a near total isotopic exchange with ice vapor, are consistent with formation at the core of the plume. Furthermore, although all spherules exhibit skeletal olivine, the substantial crystal size in SP spherules with respect to SR spherules suggests relatively slower cooling rate in the former, consistent with the slowly cooling interior of the plume.

Numerical simulations of a rocky projectile with a diameter of 100 to 150 m entering Earth's atmosphere at a velocity of 20 km s^{-1} and an impact angle from 15° to 90° show that these objects are entirely disrupted and vaporized before reaching ground level (37). Figure S7 represents a model of the thermal conditions before impact on ice of a 100-m projectile displaying the physical properties of dunite (ρ of 3.3 g cm^{-3}), which is a close analog to chondritic material. The projectile is entirely vaporized before reaching ground level by shock-heated air at ~30,000 K. However, contrary to smaller events (e.g., Tunguska), the vapor jet that is almost an order of magnitude wider than the initial body does not lose momentum and reaches the ground with a velocity of ~6 to 10 km s^{-1}, resulting in a touchdown event. At this time, its density is too low (0.1 to 0.01 g/cm^3; fig. S7) to form a regular impact crater. Instead, a major effect of a touchdown event is the interaction of a superheated vapor jet with the ground surface (fig. S8). Thermal radiation is also produced by fragmentation in airbursts and has been estimated from the energy release in atmosphere using a constant (independent of altitude and observational point) luminous efficiency of 5% (38). This burst of thermal radiation will reach the ground before the arrival of the vaporized object, potentially causing a first stage of ice vaporization. Assuming that all radiation is absorbed by the surface (albedo of 0) and that vaporization is instantaneous (i.e., we did not consider propagation of the vaporization front through ice and any other sources of energy dissipation), the ice density is 0.92 g cm^{-3}, and its heat of vaporization is 2270 J/g, we find that the maximum depth of vaporization is near the impact point (>1 cm and up to 50 cm), but in a large area, this depth does not exceed 1 mm (fig. S8, C and D). The total volume of vaporized ice is about 0.01 km^3, which is equivalent

to 12 km^3 of vapor (at atmospheric pressure and a temperature of 373 K) or to a 150-m-thick layer of vapor within 5-km radius near the impact point. If the ice albedo is 0.5 (*39*), the vaporized volume and layer thickness would be twice as small. A more accurate numerical model (*38*) shows that the thermal flux is similar to simple estimates near the impact point but drops much quicker with increasing distance (fig. S8D). As a result, the total volume of vaporized ice is six times smaller. This produces a mass of water vapor of 9.2×10^9 to 1.6×10^9 kg, releasing 4.1×10^9 to 0.71×10^9 kg of O$_2$ at 3000 K (50% dissociation), compared to 7.0×10^8 kg of O$_2$ released by vaporization of the chondritic impactor (assuming 50 wt % O) (*35*). Thus, vaporization by the thermal pulse alone produces sufficient water vapor to explain the large degrees of mixing observed.

The condensation of spherules releases additional (latent) heat into the system. On the other hand, mixing and heat exchange between melt droplets and ice are much less efficient. Subsequently, this hot mixture rises along the atmospheric wake while cooling proceeds (Fig. 5). Within 3 to 4 min, the plume, which is now a mixture of projectile material, water, and air, reaches its maximum altitude of ~400 km, by which point impact spherules have condensed (fig. S9). Last, the plume collapses back to the lower dense layer of the atmosphere, forming a spherule-rich cloud with a radius of thousands of kilometers (*37*). Such a scenario may account for a continental distribution including the Sør Rondane Mountain chain, Dome Concordia (i.e., approximately 2700 km away), and Dome Fuji that is located along a line between these two locations.

Implications for the impact cratering record and hazard

A unique characteristic of the touchdown event described here is that it occurred over the Antarctic ice sheet. The difficulty in linking a precise age to WN particles cannot exclude that the occurrence of WN, DC, and DF results from multiple touchdown events taking place within a short time window. However, the rate of impact of an asteroid ca. 10^6 kt in mass has been calculated as approximating one every 10^5 years, which strengthens our scenario of a single impact and may explain the paucity of such touchdown events in the geological record. However, should the particles represent the products of several events, this stresses the necessity for reassessing the threat of medium-sized asteroids even more. Examples of impact-derived material found in the geological record that are not associated with known craters remain rare (*2*). These include the Dakhla desert glasses, which are thought to have been produced by melting of desert surface by thermal radiation resulting from a large airburst event (*40*). The spherules described here are further unequivocal examples of impactites produced during a unique touchdown event in the geological record (*9*). It is likely that similar touchdown events vaporizing the surface of an ocean will produce similar spherules exhibiting purely meteoritic compositions [albeit with possible contamination from Na and Cl; e.g., (*20*)] and heterogeneous redox conditions producing SR and SP spherules, which are not observed in airburst residues (*7*). As a result, WN spherules may prove useful for the identification of these events in deep sea sediment cores and, if plume expansion reaches landmasses, the sedimentary record. Furthermore, cosmic spinel is known to be particularly resistant to terrestrial weathering and has long been used to characterize impact spherules. However, oxygen isotope signatures of these particles may not be distinguishable from those of airburst residues, as the target (i.e., oceanic water) δ^{18}O overlaps with that of chondrites (*41*). To complete Earth's asteroid impact record, future studies should focus on the identification of similar events on different targets (e.g., rocky or shallow oceanic basements), as the Antarctic ice sheet only covers ca. 9% of Earth's land surface.
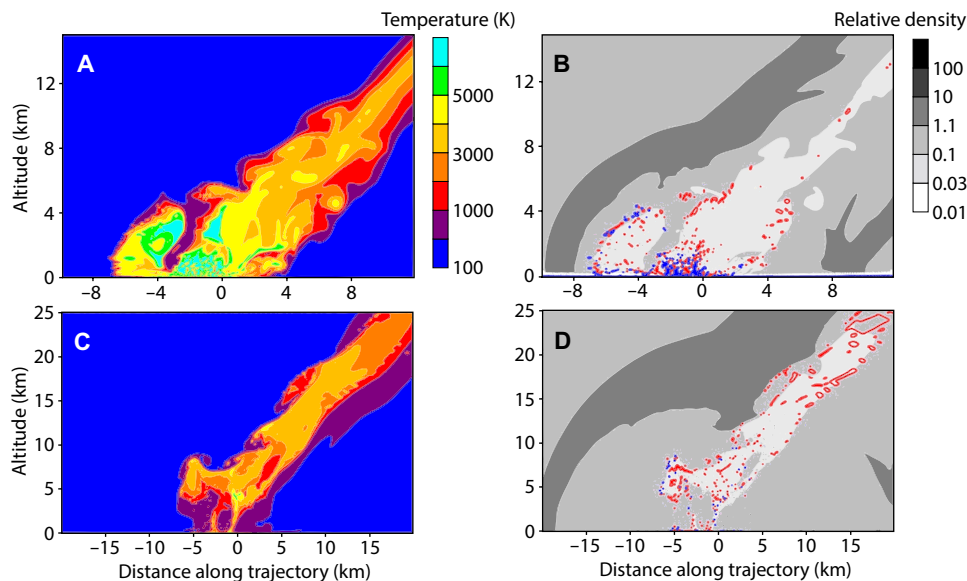
Fig. 5. Temperature and density distribution in the impact plume after the contact. (**A**) and (**B**) represent temperature and density after 10 s, respectively; (**C**) and (**D**) represent temperature and density after 36 s, respectively. Shortly after the impact of vapor jet into ice, temperature near the impact point (from −4 to 0 km along the *X* axis and up to 2-km altitude) remains extremely high. Mixing with vaporized ice (i.e., steam) occurs at this point. Thirty-six seconds after the contact, temperature drops below 3000 K; it is likely that impact spherules have condensed by that point (note, however, that the process of condensation and formation of particles is not included into the model). (B) and (D) show relative density (the ratio of the current density to the density of undisturbed atmosphere). Shock waves (dark gray areas) propagate outward from the impact point; density within the wake is below normal (vapor and air are hot). Blue/red contours show ice/projectile materials respectively. Intensive mixing takes place immediately after the impact (B); this mixture subsequently moves upward along the rarefied wake and reaches the upper troposphere during the first minute.

The impact hazards resulting from the atmospheric entry of an asteroid that are currently being addressed by impact mitigation programs depend mainly on whether the impactor reaches the ground or is entirely disrupted in the atmosphere (i.e., airburst). For small- to medium-sized impactors (50- to 150-m diameter) producing airbursts, the main hazard is limited to blast effects resulting in strong overpressures over areas of up to 100,000 km² (*37*). Thermal radiation may also result in fires over an area of 10 to 1000 km² wide (*38*). The effects of a touchdown event resulting from a projectile with a diameter of 100 m remain relatively poorly studied. Figure 5 shows that in addition to shockwaves and thermal radiation covering the aforementioned areas, these events are potentially entirely destructive over a large area, corresponding to the area of interaction between the hot jet and the ground. Touchdown events may not threaten human activity, apart from the formation of a large plume and the injection of ice crystals and impact dust in the upper atmosphere, if these occur over Antarctica. However, if a touchdown impact event takes place above a densely populated area, this would result in millions of casualties and severe damages over distances of up to hundreds of kilometers (*5*).

MATERIALS AND METHODS

Major element chemistry
Major element analyses were carried out using a JEOL JXA-8500F electron microprobe at the Museum für Naturkunde Berlin, Germany. The electron microprobe is equipped with a field emission cathode and five wavelength-dispersive spectrometers. The following experimental conditions were used:

1) 15-kV acceleration voltage, 15-nA beam current, and defocused beam of 20 μm for glass and whole-rock analyses. Bulk major analyses were determined averaging several analyses (table S1).

2) 15-kV acceleration voltage, 15-nA beam current, and spot size of 1 μm for olivine and spinel analyses.

All measured intensities were calibrated against natural minerals of the Smithsonian international standard suite and pure metals of the Astimex metal standard. Analyses were processed by the ZAF routine by the JEOL series operating system to minimize matrix effects. In addition, accuracy and reproducibility were checked regularly before and after each analysis session by measurements of minerals of the Smithsonian international standard suite.

Trace element chemistry
Uncoated sections of the particles embedded in epoxy resin were analyzed by LA-ICP-MS using the Electro Scientific Instruments New Wave UP-193FX ArF excimer (193 nm) Laser Ablation System coupled to a Thermo Electron Element XR ICP-MS at Florida State University, USA (*42–44*). Together, 76 peaks for major and trace elements and their interferences were monitored. Spot sizes of 50 μm were used, and the laser repetition rate was 50 Hz, with a fluence of >2 GW cm⁻². Laser dwell times on a spot were 10 s, resulting in a pit depth of ~50 μm. USGS glasses (BHVO-2g, BCR-2g, and BIR-1g) were used as the external standards for elements that have been precisely determined in these glasses, for example, major elements, Rb, Sr, Nb, Zr, Ba, Rare Earth Elements, Th, and U. For elements that were poorly constrained in USGS glass, such as some chalcophile and siderophile elements, NIST SRM 610 was used as the external standard. The reproducibility of major elements and most of the trace lithophile elements obtained using this technique is better than 5%.

Quantitative data for trace element concentrations of the bedrock residues from which the particles were extracted were acquired for sample powders at the Laboratoire G-Time of the Université Libre de Bruxelles (ULB), using ICP-MS. Bulk subsamples were cleaned, crushed manually, and homogenized in an agate mortar at the Analytical, Environmental and Geo-Chemistry (AMGC) laboratory of the Vrije Universiteit Brussel (VUB). Around 50 mg of powdered samples was mixed with ~1 g of a 4:1 ultrapure metaborate-tetraborate mixture. The mixture was heated in a graphite crucible at 1000°C for 10 min. After cooling down, the bead was dissolved in 50 ml of 2N HNO₃ with a stirring magnet for 5 hours. The solution was diluted accordingly for major and trace element measurements. Indium was used as internal standard for trace elements analyses, performed on an Agilent 7700 ICP-MS at Laboratoire G-Time at ULB. Yttrium was used as internal standard for major element analyses performed on a Thermo Scientific ICaP also at ULB. In both cases, the calibration curves were obtained on solutions of artificial multielement standards, while solutions prepared from natural reference material from the USGS (BHVO-2 and AGV-2) were used for quality control. The external reproducibility expressed as relative SD (RSD) is better than 5% (based on six replicates of BHVO-2) for trace elements (except Rb and Lu, 7 and 10%, respectively). The external reproducibility for major elements is better than 5% RSD (based on eight replicates of BHVO-2), except for K that is better than 10% RSD. Loss on ignition was determined after 1 hour at 500°C followed by 1 hour at 1000°C.

Oxygen isotope ratios
We measured the oxygen isotopic compositions of geochemically characterized olivine crystals with a CAMECA IMS 1270 E7 at the Centre de Recherches Pétrographiques et Géochimiques (Nancy, France). $^{16}O^-$, $^{17}O^-$, and $^{18}O^-$ ions produced by a Cs^+ primary ion beam (~10 μm and ~2 nA) were detected in multicollection mode using two off-axis Faraday cups (FCs) for $^{16}O^-$ and $^{18}O^-$ and the axial FC for $^{17}O^-$. To remove the $^{16}OH^-$ interference on the $^{17}O^-$ peak and to obtain maximum flatness on the top of the $^{16}O^-$ and $^{18}O^-$ peaks, entrance and exit slits were adjusted to acquire a mass resolving power (MRP) of ≈7000 for $^{17}O^-$ on the central FC. The multicollection FCs were set on slit 1 (MRP = 2500). The total measurement time was 270 s (180-s measurement + 90-s presputtering). We used four in-house terrestrial standard materials (San Carlos olivine, CLDR01 MORB glass, Charroy magnetite, and JV1 diopside) to (i) define the instrumental mass fractionation line for the three oxygen isotopes and (ii) to correct the instrumental mass fractionation due to the matrix effect in samples. Typical count rates obtained on the San Carlos olivine standard were 1×10^9 cps for ^{16}O, 3.5×10^5 cps for ^{17}O, and 1.8×10^6 cps for ^{18}O. The 2σ errors were ≈0.4‰ for $\delta^{18}O$, ≈0.7‰ for $\delta^{17}O$, and ≈0.8‰ for $\Delta^{17}O$ ($\Delta^{17}O$ representing the deviation from the TFL, $\Delta^{17}O = \delta^{17}O - 0.52 \times \delta^{18}O$).

Impact model
To model the impact of a 100-m asteroid, we use the SOVA hydrocode (*45*) coupled with the ANEOS equations of state for dunite (projectile) and ice (target). First, the atmospheric entry of a cosmic body was modeled in 2D (the atmospheric stratification was changed to imitate an oblique impact). Second, interaction of the projectile remnants with ice and atmosphere was modeled in 3D. Details of this approach are described in (*35*). Mixing of two materials (ice and projectile vapor) is not included in the model. The SOVA code was built to prevent mixing and numerical diffusion between different

materials. Thus, we can only hypothesize ice melting within an impact plume that is formed after the impact. There are three possible ways to vaporize the icy surface: (i) by thermal radiation emitted during the entry, (ii) by shock compression of ice during the impact, and (iii) by thermal conduction/convection/radiation within a rising plume. The main text evaluates the input from each of these processes.

SUPPLEMENTARY MATERIALS

Supplementary material for this article is available at http://advances.sciencemag.org/cgi/content/full/7/14/eabc1008/DC1

REFERENCES AND NOTES

1. G. R. Osinski, E. Pierazzo, Eds., *Impact Cratering* (John Wiley & Sons Ltd, 2012).
2. B. P. Glass, B. M. Simonson, *Distal Impact Ejecta Layers* (Springer Berlin Heidelberg, 2013).
3. N. A. Artemieva, V. V. Shuvalov, From Tunguska to Chelyabinsk via Jupiter. *Annu. Rev. Earth Planet. Sci.* **44**, 37–56 (2016).
4. P. G. Brown, J. D. Assink, L. Astiz, R. Blaauw, M. B. Boslough, J. Borovička, N. Brachet, D. Brown, M. Campbell-Brown, L. Ceranna, W. Cooke, C. de Groot-Hedlin, D. P. Drob, W. Edwards, L. G. Evers, M. Garces, J. Gill, M. Hedlin, A. Kingery, G. Laske, A. Le Pichon, P. Mialle, D. E. Moser, A. Saffer, E. Silber, R. E. Spalding, P. Spurný, E. Tagliaferri, D. Uren, R. J. Weryk, R. Whitaker, Z. Krzeminski, A 500-kiloton airburst over Chelyabinsk and an enhanced hazard from small impactors. *Nature* **503**, 238–241 (2013).
5. M. B. E. Boslough, D. A. Crawford, Low-altitude airbursts and the impact threat. *Int. J. Impact Eng.* **35**, 1441–1448 (2008).
6. P. A. Bland, N. A. Artemieva, The rate of small impacts on Earth. *Meteorit. Planet. Sci.* **41**, 607–631 (2006).
7. M. van Ginneken, L. Folco, N. Perchiazzi, P. Rochette, P. A. Bland, Meteoritic ablation debris from the Transantarctic Mountains: Evidence for a Tunguska-like impact over Antarctica ca. 480ka ago. *Earth Planet. Sci. Lett.* **293**, 104–113 (2010).
8. B. Narcisi, J. R. Petit, C. Engrand, First discovery of meteoritic events in deep Antarctic (EPICA-Dome C) ice cores. *Geophys. Res. Lett.* **34**, L15502 (2007).
9. K. Misawa, M. Kohno, T. Tomiyama, T. Noguchi, T. Nakamura, K. Nagao, T. Mikouchi, K. Nishiizumi, Two extraterrestrial dust horizons found in the Dome Fuji ice core, East Antarctica. *Earth Planet. Sci. Lett.* **289**, 287–297 (2010).
10. M. J. Genge, C. Engrand, M. Gounelle, S. Taylor, The classification of micrometeorites. *Meteorit. Planet. Sci.* **43**, 497–515 (2008).
11. C. Cordier, M. Van Ginneken, L. Folco, Nickel abundance in stony cosmic spherules: Constraining precursor material and formation mechanisms. *Meteorit. Planet. Sci.* **46**, 1110–1132 (2011).
12. A. Toppani, G. Libourel, Factors controlling compositions of cosmic spinels: Application to atmospheric entry conditions of meteoritic materials. *Geochim. Cosmochim. Acta* **67**, 4621–4638 (2003).
13. R. N. Clayton, T. K. Mayeda, D. E. Brownlee, Oxygen isotopes in deep-sea spherules. *Earth Planet. Sci. Lett.* **79**, 235–240 (1986).
14. J. Gayraud, E. Robin, R. Rocchia, L. Froget, *The Cretaceous-Tertiary Event and Other Catastrophes in Earth History* (Geological Society of America, 1996).
15. E. Robin, P. Bonté, L. Froget, C. Jéhanno, R. Rocchia, Formation of spinels in cosmic objects during atmospheric entry: A clue to the Cretaceous-Tertiary boundary event. *Earth Planet. Sci. Lett.* **108**, 181–190 (1992).
16. E. Robin, E. Molina, Chronostratigraphy, composition, and origin of Ni-rich spinel from the Late Eocene Fuente Caldera section in Spain: One impact or more? *Meteorit. Planet. Sci.* **41**, 1231–1248 (2006).
17. G. R. Byerly, D. R. Lowe, Spinel from Archean impact spherules. *Geochim. Cosmochim. Acta* **58**, 3469–3486 (1994).
18. F. T. Kyte, J. A. Bostwick, Magnesioferrite spinel in Cretaceous/Tertiary boundary sediments of the Pacific basin: Remnants of hot, early ejecta from the Chicxulub impact? *Earth Planet. Sci. Lett.* **132**, 113–127 (1995).
19. S. V. Margolis, P. Claeys, F. T. Kyte, Microtektites, microkrystites, and spinels from a late pliocene asteroid impact in the Southern Ocean. *Science* **251**, 1594–1597 (1991).
20. F. T. Kyte, Composition of impact melt debris from the Eltanin impact strewn field, Bellingshausen Sea. *Deep Sea Res. II Top. Stud. Oceanogr.* **49**, 1029–1047 (2002).
21. L. Folco, P. Rochette, N. Perchiazzi, M. D'Orazio, M. A. Laurenzi, M. Tiepolo, Microtektites from Victoria Land Transantarctic Mountains. *Geology* **36**, 291–294 (2008).
22. B. P. Glass, Tektites and microtektites: Key facts and inferences. *Tectonophysics* **171**, 393–404 (1990).
23. P. Rochette, L. Folco, C. Suavet, M. van Ginneken, J. Gattacceca, N. Perchiazzi, R. Braucher, R. P. Harvey, Micrometeorites from the Transantarctic Mountains. *Proc. Natl. Acad. Sci. U.S.A.* **105**, 18206–18211 (2008).
24. R. P. Harvey, N. W. Dunbar, R. P. Esser, W. C. McIntosh, K. Nishiizumi, S. Taylor, M. W. Caffee, Meteoritic event recorded in Antarctic ice. *Geology* **26**, 607–610 (1998).
25. Y. Suganuma, H. Miura, A. Zondervan, J. Okuno, East Antarctic deglaciation and the link to global cooling during the Quaternary: Evidence from glacial geomorphology and 10Be surface exposure dating of the Sør Rondane Mountains, Dronning Maud Land. *Quat. Sci. Rev.* **97**, 102–120 (2014).
26. Dome Fuji Ice Core Project Members, K. Kawamura, A. Abe-Ouchi, H. Motoyama, Y. Ageta, S. Aoki, N. Azuma, Y. Fujii, K. Fujita, S. Fujita, K. Fukui, T. Furukawa, A. Furusaki, K. Goto-Azuma, R. Greve, M. Hirabayashi, T. Hondoh, A. Hori, S. Horikawa, K. Horiuchi, M. Igarashi, Y. Iizuka, T. Kameda, H. Kanda, M. Kohno, T. Kuramoto, Y. Matsushi, M. Miyahara, T. Miyake, A. Miyamoto, Y. Nagashima, Y. Nakayama, T. Nakazawa, F. Nakazawa, F. Nishio, I. Obinata, R. Ohgaito, A. Oka, J. Okuno, J. Okuyama, I. Oyabu, F. Parrenin, F. Pattyn, F. Saito, T. Saito, T. Saito, T. Sakurai, K. Sasa, H. Seddik, Y. Shibata, K. Shinbori, K. Suzuki, T. Suzuki, A. Takahashi, K. Takahashi, S. Takahashi, M. Takata, Y. Tanaka, R. Uemura, G. Watanabe, O. Watanabe, T. Yamasaki, K. Yokoyama, M. Yoshimori, T. Yoshimoto, State dependence of climatic instability over the past 720,000 years from Antarctic ice cores and climate modeling. *Sci. Adv.* **3**, e1600446 (2017).
27. R. N. Clayton, T. K. Mayeda, Oxygen isotope studies of carbonaceous chondrites. *Geochim. Cosmochim. Acta* **63**, 2089–2104 (1999).
28. R. N. Clayton, T. K. Mayeda, J. N. Goswami, E. J. Olsen, Oxygen isotope studies of ordinary chondrites. *Geochim. Cosmochim. Acta* **55**, 2317–2337 (1991).
29. J. Newton, I. A. Franchi, C. T. Pillinger, The oxygen-isotopic record in enstatite meteorites. *Meteorit. Planet. Sci.* **35**, 689–698 (2000).
30. M. van Ginneken, M. J. Genge, L. Folco, R. P. Harvey, The weathering of micrometeorites from the Transantarctic Mountains. *Geochim. Cosmochim. Acta* **179**, 1–31 (2016).
31. S. Goderis, B. Soens, M. S. Huber, M. McKibbin, M. van Ginneken, F. Van Maldeghem, V. Debaille, R. C. Greenwood, I. A. Franchi, V. Cnudde, S. Van Malderen, F. Vanhaecke, C. Koeberl, D. Topa, P. Claeys, Cosmic spherules from Widerøefjellet, Sør Rondane Mountains (East Antarctica). *Geochim. Cosmochim. Acta* **270**, 112–143 (2020).
32. M. H. Thiemens, T. Jackson, E. C. Zipf, P. W. Erdman, C. van Egmond, Carbon dioxide and oxygen isotope anomalies in the mesosphere and stratosphere. *Science* **270**, 969–972 (1995).
33. M. Van Ginneken, C. Suavet, C. Cordier, L. Folco, P. Rochette, C. Sonzogni, N. Perchiazzi, Oxygen isotope composition of meteoritic ablation debris from the Transantarctic Mountains: Constraining the parent body and implications for the impact scenario. *Meteorit. Planet. Sci.* **47**, 1738–1747 (2012).
34. R. Brett, M. Sato, Intrinsic oxygen fugacity measurements on seven chondrites, a pallasite, and a tektite and the redox state of meteorite parent bodies. *Geochim. Cosmochim. Acta* **48**, 111–120 (1984).
35. R. Z. Aminov, A. A. Gudym, Equations for calculating the properties of dissociated steam. *Therm. Eng.* **64**, 597–603 (2017).
36. B. Xiao, L. Stixrude, Critical vaporization of MgSiO3. *Proc. Natl. Acad. Sci. U.S.A.* **115**, 5371–5376 (2018).
37. N. Artemieva, V. Shuvalov, Atmospheric shock waves after impacts of cosmic bodies up to 1000 m in diameter. *Meteorit. Planet. Sci.* **54**, 592–608 (2019).
38. V. V. Svetsov, V. V. Shuvalov, Thermal radiation and luminous efficiency of superbolides. *Earth Planet. Sci. Lett.* **503**, 10–16 (2018).
39. S. G. Warren, R. E. Brandt, T. C. Grenfell, Visible and near-ultraviolet absorption spectrum of ice from transmission of solar radiation into snow. *Appl. Optics* **45**, 5320–5334 (2006).
40. G. R. Osinski, J. Kieniewicz, J. R. Smith, M. B. E. Boslough, M. Eccleston, H. P. Schwarcz, M. R. Kleindienst, A. F. C. Haldemann, C. S. Churcher, The Dakhleh Glass: Product of an impact airburst or cratering event in the Western Desert of Egypt? *Meteorit. Planet. Sci.* **43**, 2089–2107 (2008).
41. G. A. Schmidt, G. R. Bigg, E. J. Rohling, "Global Seawater Oxygen-18 Database - v1.22," 1999; https://data.giss.nasa.gov/o18data/.
42. M. Humayun, F. A. Davis, M. M. Hirschmann, Major element analysis of natural silicates by laser ablation ICP-MS. *J. Anal. At. Spectrom* **25**, 998–1005 (2010).
43. S. Yang, M. Humayun, K. Righter, G. Jefferson, D. Fields, A. J. Irving, Siderophile and chalcophile element abundances in shergottites: Implications for Martian core formation. *Meteorit. Planet. Sci.* **50**, 691–714 (2015).
44. S. Yang, M. Humayun, V. J. M. Salters, Elemental systematics in MORB glasses from the mid-Atlantic ridge. *Geochem. Geophys. Geosyst.*. **19**, 4236–4259 (2018).
45. V. V. Shuvalov, Multi-dimensional hydrodynamic code SOVA for interfacial flows: Application to the thermal layer effect. *Shock Waves* **9**, 381–390 (1999).
46. W. F. McDonough, S.-S. Sun, The composition of the Earth. *Chem. Geol.* **120**, 223–253 (1995).
47. K. Lodders, Solar system abundances and condensation temperatures of the elements. *Astrophys. J.* **591**, 1220–1247 (2003).
48. C. Engrand, B. Narcisi, J.-R. Petit, E. Dobrica, J. Duprat, "Lunar and Planetary Science Conference," in *Lunar and Planetary Science Conference* (Lunar and Planetary Institute, 2010), p. 1981.

49. T. Sakurai, H. Chosrowjan, T. Somekawa, M. Fujita, H. Motoyama, O. Watanabe, Y. Izawa, Studies of melting ice using CO2 laser for ice drilling. *Cold Reg. Sci. Technol.* **121**, 11–15 (2016).

50. R. G. Kraus, L. E. Senft, S. T. Stewart, Impacts onto H2O ice: Scaling laws for melting, vaporization, excavation, and final crater size. *Icarus* **214**, 724–738 (2011).

51. S. Goderis, R. Tagle, J. Belza, J. Smit, A. Montanari, F. Vanhaecke, J. Erzinger, P. Claeys, Reevaluation of siderophile element abundances and ratios across the Cretaceous–Paleogene (K–Pg) boundary: Implications for the nature of the projectile. *Geochim. Cosmochim. Acta* **120**, 417–446 (2013).

52. M. Fischer-Gödde, H. Becker, F. Wombacher, Rhodium, gold and other highly siderophile element abundances in chondritic meteorites. *Geochim. Cosmochim. Acta* **74**, 356–379 (2010).

53. S. R. Taylor, S. M. McLennan, *The Continental Crust: Its Composition and Evolution* (Blackwell Scientific Publication, 1985).

54. S. Goderis, A. D. Brandon, B. Mayer, M. Humayun, Osmium isotopic homogeneity in the CK carbonaceous chondrites. *Geochim. Cosmochim. Acta* **216**, 8–27 (2017).

55. D. S. Ebel, L. Grossman, Spinel-bearing spherules condensed from the Chicxulub impact-vapor plume. *Geology* **33**, 293–296 (2005).

Citation: M. Van Ginneken, S. Goderis, N. Artemieva, V. Debaille, S. Decrée, R. P. Harvey, K. A. Huwig, L. Hecht, S. Yang, F. E. D. Kaufmann, B. Soens, M. Humayun, F. Van Maldeghem, M. J. Genge, P. Claeys, A large meteoritic event over Antarctica ca. 430 ka ago inferred from chondritic spherules from the Sør Rondane Mountains. *Sci. Adv.* **7**, eabc1008 (2021).

Science Advances

A large meteoritic event over Antarctica ca. 430 ka ago inferred from chondritic spherules from the Sør Rondane Mountains

M. Van GinnekenS. GoderisN. ArtemievaV. DebailleS. DecréeR. P. HarveyK. A. HuwigL. HechtS. YangF. E. D. KaufmannB. SoensM. HumayunF. Van MaldeghemM. J. GengeP. Claeys

View the article online
https://www.science.org/doi/10.1126/sciadv.abc1008
Permissions
https://www.science.org/help/reprints-and-permissions

Use of think article is subject to the Terms of service